Correlation between bulk thermodynamic measurements and the low temperature resistance plateau in SmB_6

W. A. Phelan,[1,2] S. M. Koohpayeh,[2] P. Cottingham,[1,2] J. W. Freeland,[3] J. C. Leiner,[4] C. L. Broholm,[2] and T. M. McQueen[1,2*]

[1]*Department of Chemistry, Johns Hopkins University, Baltimore, Maryland 21218, USA*
[2]*Institute for Quantum Matter, Department of Physics and Astronomy, Johns Hopkins University, Baltimore, Maryland 21218, USA*
[3]*Advanced Photon Source, Argonne National Laboratory, Argonne, Illinois 60439, USA*
[4]*Quantum Condensed Matter Division, Oak Ridge National Laboratory, Oak Ridge, Tennessee 37831, USA*

[*]*mcqueen@jhu.edu*

FIG. S1. Seebeck (S) coefficient vs. temperature for the carbon-containing sample SmB_6/C-4. The orange circles correspond to the original data set in the manuscript (FIG. 3.). The dataset represented by the black circles was collected after removing all original contacts of SmB_6/C-4, repolishing of the sample, and attaching of new electrical and thermal contacts. This demonstrates the reproducibility of our measurements of $T_{S=0}$.

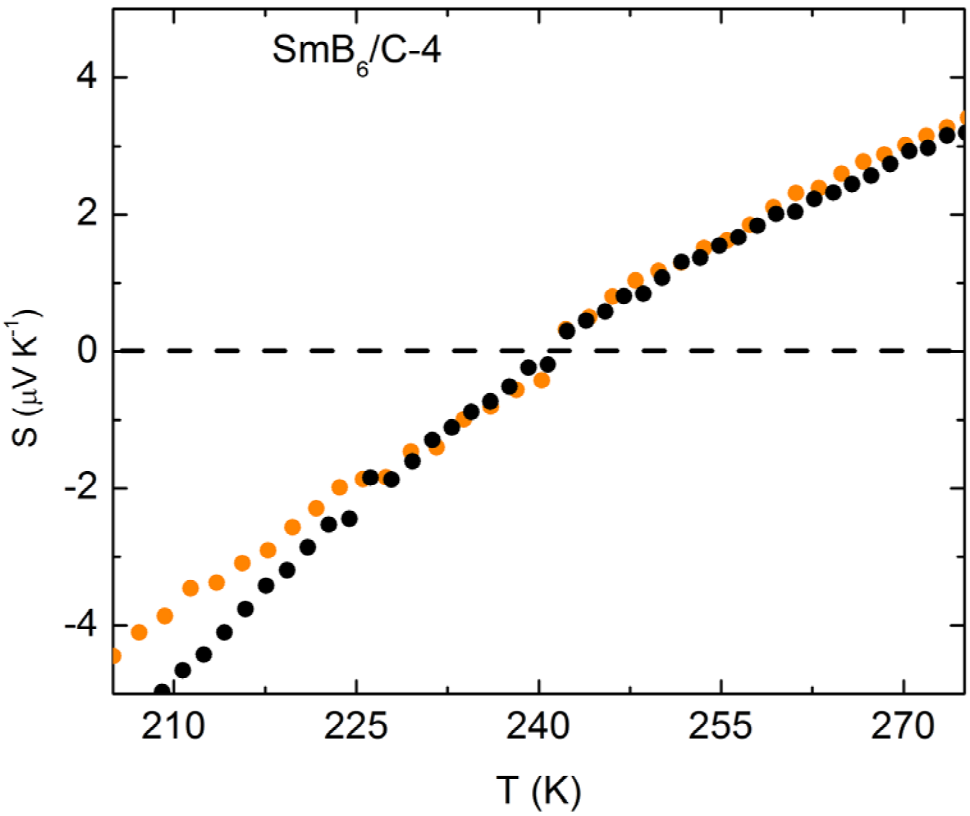

FIG. S2. Magnetization as a function of applied magnetic field at T = (a) 2 K, (b) 20 K, and (c) 200 K. The insets highlight the low applied magnetic field regions.

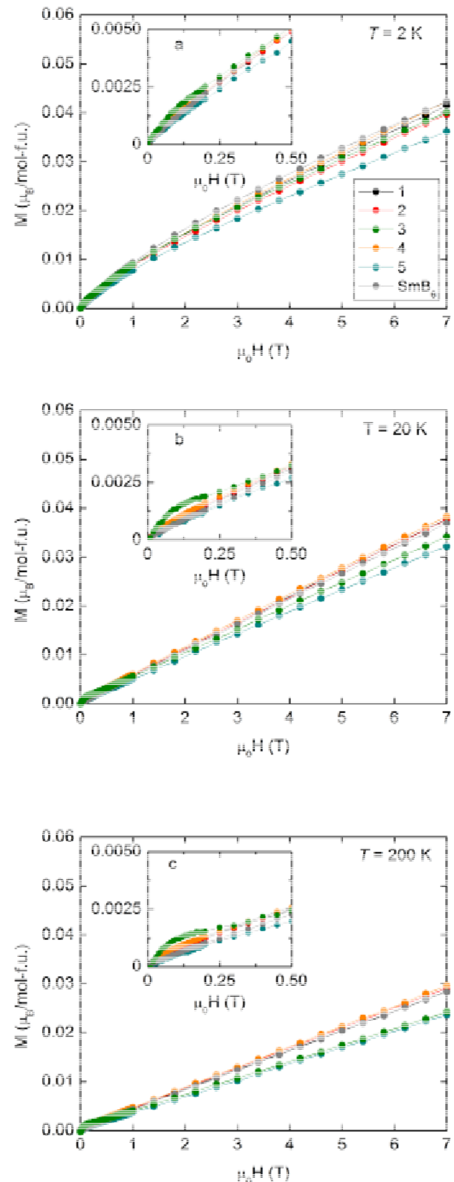

FIG. S3. Specific heat divided by temperature for SmB_6/C-5 at $\mu_0 H = 9$ *T*. The data $T \leq 10$ K were fit (shown in red) to the expression $C_p T^{-1} = \gamma + \beta T^2 + AT^2 \ln(T) + BT^{-3}$. The fit parameters can be found in Table 1 of the manuscript. The electronic, lattice, and Schottky contributions to the fit are shown as black, gray, and green curves, respectively.

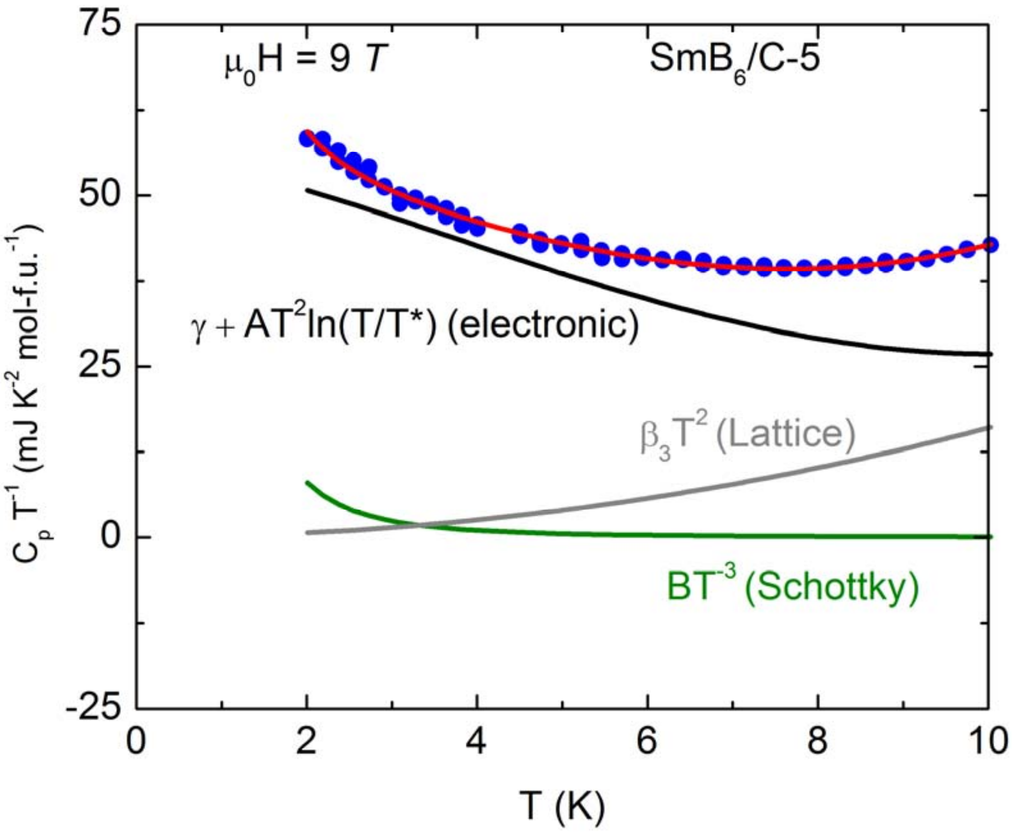

FIG. S4. Activation energy plots of the normalized resistance (a) SmB_6 and SmB_6/Al and (b) SmB_6/C. The slope of the low temperature resistance changes systematically with carbon number, but not aluminum number.

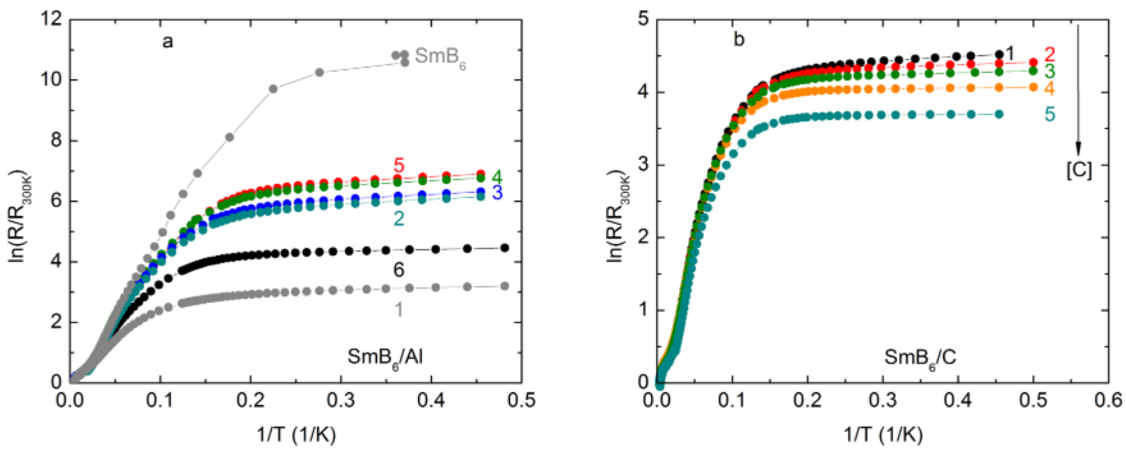

FIG. S5. (a) R/R_{10K} versus temperature for SmB_6 sample measured at excitation currents of 50 μA (black) and 5000 μA (red). (b) Excitation current versus voltage for SmB_6 in the T = 1.95 – 10 K range. The I-V curves become progressively nonlinear with decreasing temperature. (c) The resistance divided by the resistance in the limit that the excitation goes to zero ($R/R_{I\rightarrow 0}$) versus applied power for two different SmB_6 samples at T = 1.95 K. The true resistance of the black curve is approximately five times greater that of the red curve, but the downturn occurs at similar applied power, implying a Joule heating effect rather than the "turn on" of a second conduction channel (e.g. sliding charge density wave).

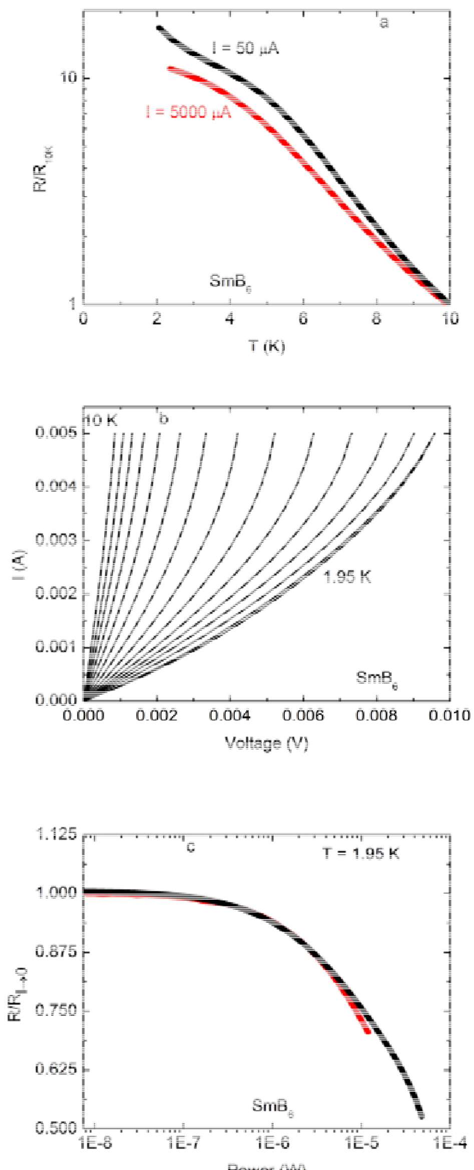

FIG. S6. As an additional check that the data presented in FIG. 2 are not contaminated by Joule heating effects, here we compare the measured resistance curves at the indicated excitation currents with the resistance values extracted from the IV curves extrapolated to the zero-current (no Joule heating) limit. The two methods of obtaining the resistances are in remarkable agreement, and imply Joule heating is not a significant contributor to the trends observed in the data in FIG. 2.

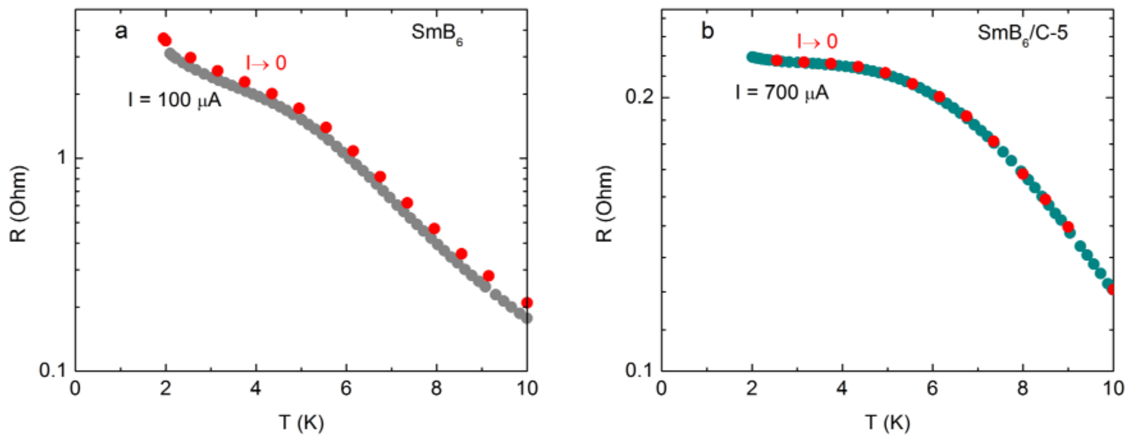

FIG. S7. Two-probe measurements to characterize the inner (R_{23}) and outer (R_{14}) contact resistances on representative specimens. These data imply contact resistances on the scale of R = 10-40 Ω, and suggest that both the sample and the contacts contribute to the Joule heating effects noted in Fig. S5.

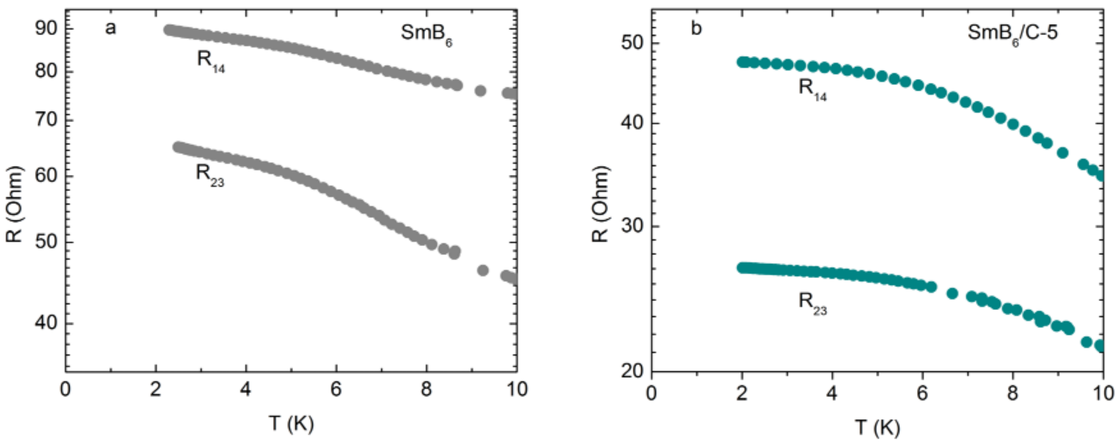

Table SI. Parameters extracted from fits to the resistance ($2 < T < 50$ K) of SmB_6, SmB_6/C-1-5, SmB_6/Al-1-6. Model fits to data were performed using the expression $R_1R_2/R_1+R_2 = (R_SR_Be^{\Delta1/2T}e^{\Delta2/2T})/(R_Se^{\Delta1/2T} +R_Be^{\Delta2/2T})$.

	R_S (Ω)	R_B (Ω)	Δ_1 (K)	Δ_2 (K)
SmB_6	8(3)	0.002(5)	16(4)	86(24)
SmB_6/C-1	0.0280(3)	0.00048(2)	1.68(6)	82(1)
SmB_6/C-2	0.0742(7)	0.00117(6)	1.04(6)	83(1)
SmB_6/C-3	0.0636(6)	0.0011(5)	0.80(6)	85(1)
SmB_6/C-4	0.0488(4)	0.00089(4)	0.48(6)	87(1)
SmB_6/C-5	0.063(7)	0.00131(6)	0.44(6)	87(1)
SmB_6/Al-1	0.0748(7)	0.0049(1)	1.96(6)	67(1)
SmB_6/Al-2	0.116(1)	0.00084(5)	3.60(6)	74.6(8)
SmB_6/Al-3	0.0691(7)	0.00048(3)	3.56(6)	75(1)
SmB_6/Al-4	0.0166(1)	0.00081(5)	3.50(4)	74.4(8)
SmB_6/Al-5	0.268(2)	0.00102(5)	3.52(4)	75.4(6)
SmB_6/Al-6	0.0367(3)	0.00066(2)	1.56(4)	73.2(6)

Table SII. Curie Constant extracted from linear fits to the slope of the H/M versus temperature data (100 < T < 300 K) of SmB_6, SmB_6/C-1-5.

	Curie Constant (cm^3/K mol-f.u.)
SmB_6	1.703(5)
SmB_6/C-1	1.761(3)
SmB_6/C-2	1.724(6)
SmB_6/C-3	1.835(7)
SmB_6/C-4	1.783(7)
SmB_6/C-5	1.852(7)

Table SIII. Parameters extracted from fits to the low temperature specific heat ($2 < T < 10$ K) of SmB_6, SmB_6/C-1, SmB_6/C-2, SmB_6/C-3, and SmB_6/C-5 under various applied magnetic fields. Model fits to the specific heat data were performed using the expression $C_p/T = \gamma + \beta T^2 + AT^2\ln(T) + BT^{-3}$. The individual terms are defined in the text. An example fit is shown in Fig. S3. Test fits of the pure and SmB6/C-5 samples over different temperature ranges (T = 3 to 12 K, 2 to 12 K) show that while there is some variability in the precise values of ß and A depending on the range used, they still follow the universal relationship presented Fig. 6, and the values of γ change by at most 10-15%.

	Field	γ (mJ K^2 mol-f.u^{-1})	β (mJ K^{-4} mol-f.u^{-1})	A (mJ K^{-4} mol-f.u^{-1})	B (mJ K mol-f.u $^{-1}$)
SmB_6	0 *T*	24.8(6)	0.45(6)	-0.10(3)	66(5)
	3 *T*	28.6(3)	0.19(3)	-0.01(1)	65(3)
	5 *T*	29.2(3)	0.22(3)	-0.02(1)	52(3)
	9 *T*	29.4(4)	0.25(4)	-0.03(2)	56(3)
SmB_6/C-1	0 *T*	48.3(3)	-0.70(3)	0.30(1)	40(2)
	3 *T*	51.3(2)	-0.88(2)	0.37(1)	44(2)
	5 *T*	52.4(2)	-0.90(2)	0.37(1)	35(2)
	9 *T*	54.4(2)	-0.99(2)	0.41(1)	33(2)
SmB_6/C-2	0 *T*	46.6(3)	-0.96(3)	0.40(1)	55(3)
	3 *T*	49.0(4)	-1.07(4)	0.44(2)	64(4)
	5 *T*	49.2(4)	-1.02(4)	0.41(2)	65(4)
	9 *T*	51.7(4)	-1.16(5)	0.47(2)	59(4)
SmB_6/C-3	0 *T*	49.6(9)	-1.07(9)	0.44(3)	59(7)
	3 *T*	51.7(3)	-1.19(3)	0.48(1)	67(2)
	5 *T*	52.7(3)	-1.20(3)	0.49(1)	58(2)
	9 *T*	54.7(3)	-1.28(3)	0.51(1)	56(2)
SmB_6/C-5	0 *T*	47.7(2)	-1.02(3)	0.41(1)	83(2)
	3 *T*	53.0(3)	-1.38(4)	0.55(1)	74(3)
	5 *T*	53.8(3)	-1.38(3)	0.55(1)	68(2)
	9 *T*	55.6(4)	-1.44(5)	0.57(2)	64(4)

Extraction of Magnetic Moment Information from Surface XMCD

The extraction of magnetic moment information from the surface XMCD data was performed following the same procedure as that reported by Dhesi, et al. for $SmAl_2$ [1]. A linear background was removed from the XAS spectrum prior to integration. We assumed that the X_I/X_E ratio [2] for the MCD sum rule was 3.0, and that the ratio $\langle T_z \rangle / \langle S_z \rangle = -0.2$ [3].

Supplementary References

[1] S. S. Dhesi, G. van der Laan, P. Bencok, N. B. Brookes, R. M. Galera, and P. Ohresser, Spin- and orbital-moment compensation in the zero-moment ferromagnet $Sm_{0.974}Gd_{0.026}Al_2$, Phys. Rev. B: Condens. Matter **82**, 180402, 180402 (2010).

[2] T. Jo, The 3d–4f exchange interaction, X-ray second-order optical processes and the magnetic circular dichroism (MCD) spin sum rule in rare earths, J. Electron. Spectrosc. Relat. Phenom. **86**, 73 (1997).

[3] P. Carra, B. T. Thole, M. Altarelli, and X. Wang, X-ray circular dichroism and local magnetic fields, Phys. Rev. Lett. **70**, 694 (1993).